Kleber Marques Lisboa
Laboratory of Thermal Sciences (LATERMO),
Department of Mechanical Engineering
(TEM/PGMEC),
Universidade Federal Fluminense, UFF,
Niterói,
Rio de Janeiro CEP 24.210-240, Brazil
e-mail: kmlisboa@id.uff.br

Isabela Florindo Pinheiro
Laboratory of Thermal Sciences (LATERMO),
Department of Mechanical Engineering
(TEM/PGMEC),
Universidade Federal Fluminense, UFF,
Niterói,
Rio de Janeiro CEP 24.210-240, Brazil
e-mail: isabelaflorindo@id.uff.br

Renato Machado Cotta[1]
Laboratory of Nano and Microfluidics and
Microsystems, LabMEMS,
Mechanical Engineering Department,
POLI and COPPE,
Federal University of Rio de Janeiro, UFRJ,
Rio de Janeiro CEP 21.941-594, Brazil;
Laboratory of Sustainable Energies
Technologies,
LATES-IPqM,
General Directorate of Nuclear and Technological
Development, DGDNTM,
Brazilian Navy,
Rio de Janeiro CEP 21.931-095, Brazil
e-mail: cotta@mecanica.coppe.ufrj.br

Integral Transform Solution of Porous Medium Models for Heat Sinks Subject to Periodic Heat Loads

Analysis of the energy transport in thermal microdevices modeled as a porous medium under periodic heat loads is conducted using integral transforms. Coupled eigenvalue problems are employed and a single set of coupled ordinary differential equations conveying all information on the temperature fields in both the solid and fluid phases are reached, allowing for a relatively straightforward treatment of the local thermal nonequilibrium (LTNE) formulation. This characteristic proved instrumental in finding out that the local thermal equilibrium (LTE) hypothesis is inadequate for unsteady problems. The solid phase is shown to have a significant role on inducing thermal lag in the fluid, which may be severe, depending on the dimensions and operational conditions. In general, devices comprised of larger fractions of solid material and with poorer heat transfer characteristics are more prone to having larger thermal lag along them. These conclusions may be relevant to a wide range of applications such as electronics cooling, battery thermal management, solar energy harvesting, among others. [DOI: 10.1115/1.4056003]

Keywords: porous media, thermal lag, periodic heat loads, thermal microdevices, integral transforms, generalized integral transform technique

Introduction

Transport process intensification is one of the main strategies for improving the energy efficiency of industrial equipment, and advances in this area can certainly aid in the energy transition efforts. Such processes are mostly surface-based, meaning that greater area-to-volume ratios directly translate into better performance of the devices involved. Notably, research and development of thermal devices have been pursuing miniaturization as a mean of boosting this ratio for a while [1], with remarkable results in cooling of electronics [2,3] and high concentration photovoltaic cells [4], waste heat recovery [5], heat pipes [6,7], among others.

Several challenges arise when numerically analyzing miniaturized thermal devices due to their inherent multiscale nature, requiring refined enough meshes around the smallest structures and, thus, leading to very time-consuming computations. Professor Catton and his collaborators were among the firsts to recognize the potential of employing the volume averaging technique to produce an upscaled model where small-scale information is incorporated into the equations through properly modeled effective properties of a fluid saturated porous medium [8–11], allowing for more effective simulation and optimization of these devices. This strategy is often referred to as "designed porous medium" [12] and it has recently been applied to the thermodynamic optimization of several microscale geometries of heat sinks intended for low-grade waste heat recovery applications [13].

Many studies have dealt with conjugate heat transfer in thermal devices modeled as porous media by adopting the local thermal equilibrium (LTE) hypothesis, i.e., assuming that, in each representative elementary volume, the solid and fluid phases temperatures are equal on average [14–16]. This approach is appealing, since it leads to a single equation encompassing all heat transfer information, simplifying the simulation process. However, prescribed heat loads, significant differences in thermophysical properties, and unsteady conditions are known to induce significant deviations from the LTE hypothesis, requiring a two-equation alternative to be used instead, in what is called the local thermal nonequilibrium (LTNE) formulation [17–22].

Analyses of heat transfer in microdevices are usually restricted to steady-state. Nevertheless, most applications involve transient periods that might affect the overall performance of the equipment. For instance, computer processors can boost their frequency for short periods of time to deal with highly demanding tasks, and any cooling device attached to it must be capable of promptly responding to this temporary additional heat load to avoid overheating of the integrated circuits. A relevant subset of time-dependent behavior is the periodic one, occurring when a thermal device is subjected to a periodic heat load for a time long enough for the initial transient to die out and the temperature field within the device to start oscillating with the same frequency of the heat load [23,24]. This situation is representative of applications such as thermal comfort [25,26], where thermal lag is leveraged to ease out day-wise temperature variation, battery charge–discharge cycles [27,28], and solar energy (either thermal or photovoltaic) harvesting [29,30].

The generalized integral transform technique (GITT) [31,32] was proposed in the 1980s as an extension of the classical integral transform technique [33] to enable the hybrid

[1]Corresponding author.

Contributed by the Heat Transfer Division of ASME for publication in the Journal of Heat and Mass Transfer. Manuscript received August 1, 2022; final manuscript received October 8, 2022; published online December 19, 2022. Assoc. Editor: Antonio Barletta.

numerical–analytical solution of partial differential equations involving nontransformable terms. Since then, this approach has evolved enough to deal with a plethora of problems within the fluid flow and convection–diffusion realms such as heat transfer in irregular geometries [34–37], nonlinear problems [31,38–41], and the Navier–Stokes equations [42–45], combining the flexibility of numerical schemes with the reliability and robustness of analytical methods. In particular, heat and fluid flow in porous media were tackled by the GITT in several efforts [46–48] and, recently, an extension of the so-called class IV problems solution [33] was shown to successfully handle LTNE formulations for roughly the same computational cost of adopting the more limited LTE hypothesis [13,49].

In this work, the unsteady thermal response of a fluid flow through a porous channel subjected to a periodic heat flux at the bottom is evaluated. Adopting the designed porous medium framework, a microchannels-based thermal device is analyzed with an upscaled LTNE model and chosen as a base case from which relevant dimensionless parameters are varied to probe their effect on the thermal lag of both the solid and liquid phases within the porous channel. The GITT is chosen as the solution method for its recently found capability of handling LTNE formulations effectively in combination with symbolic computation provided by the Wolfram Mathematica platform [50].

Model and Methods

Figure 1 illustrates a porous channel insulated at the top and with a periodic heat flux imposed at the bottom. A fluid flows through and saturates the porous medium with a velocity u, assumed to be constant along the y-direction (Darcy flow hypothesis). The porous medium height is d and its width is assumed to be large enough so that the temperature fields are invariant along the transversal z-direction. As already pointed out, this porous channel can effectively represent microdevices, provided models to upscale the effects of the smallest structures are available [8–13].

In applications involving microdevices, the thermophysical properties of the solid and fluid phases may differ considerably. Furthermore, unsteady heat transfer problems are known to not be amenable to the simpler LTE formulation [18], thus, the two-equation LTNE model is adopted as follows [9–11]:

$$(1-\varepsilon)(\rho c_p)_s \frac{\partial T_s}{\partial t} = k_s(1-\varepsilon)\left[\frac{\partial^2 T_s}{\partial x^2} + \frac{\partial^2 T_s}{\partial y^2}\right] - a_{fs}h_{fs}(T_s - T_f) \tag{1a}$$

$$\varepsilon(\rho c_p)_f \frac{\partial T_f}{\partial t} + (\rho c_p)_f u \frac{\partial T_f}{\partial x} = k_f \varepsilon\left[\frac{\partial^2 T_f}{\partial x^2} + \frac{\partial^2 T_f}{\partial y^2}\right] - a_{fs}h_{fs}(T_f - T_s) \tag{1b}$$

with boundary conditions and heat flux given by

$$T_s(0,y,t) = T_f(0,y,t) = T_{\text{in}} \tag{1c,d}$$

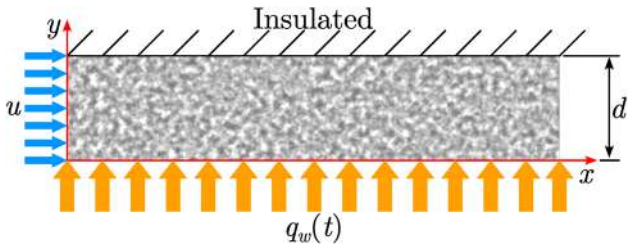

Fig. 1 Schematic of the fluid saturated porous channel subjected to a periodic heat flux at the bottom. A Cartesian coordinate system and relevant quantities are included to ease the understanding of the model.

$$\left|\frac{\partial T_f}{\partial x}\right|_{x\to\infty} < \infty \tag{1e}$$

$$\left|\frac{\partial T_s}{\partial x}\right|_{x\to\infty} < \infty \tag{1f}$$

$$T_f(x,0,t) = T_s(x,0,t) \tag{1g}$$

$$q_w(t) = -k_s(1-\varepsilon)\frac{\partial T_s}{\partial y}_{y=0} - k_f\varepsilon\frac{\partial T_f}{\partial y}\Big|_{y=0} \tag{1h}$$

$$\left.\frac{\partial T_f}{\partial y}\right|_{y=d} = \left.\frac{\partial T_s}{\partial y}\right|_{y=d} = 0 \tag{1i,j}$$

$$q_w(t) = q_{w,0}\cos(\omega t) \tag{1k}$$

where x and y are the horizontal and vertical coordinates, t is the time, T_s and T_f are the intrinsic average temperatures of the solid and fluid phases, respectively, T_{in} is the inlet temperature, $(\rho c_p)_s$ and $(\rho c_p)_f$ are the thermal capacities of the solid and fluid phases, respectively, k_s and k_f are the thermal conductivities of the solid and fluid phases, respectively, ε is the porosity of the porous medium, a_{fs} is the specific surface area of the porous medium, h_{fs} is the interstitial heat transfer coefficient, q_w is the imposed heat flux, and $q_{w,0}$ and ω are, respectively, the amplitude and angular frequency of the prescribed wall heat flux.

A bounded gradient along the x-direction is imposed as $x \to \infty$ in Eqs. (1*e*) and (1*f*) for reasons to be clarified further in the text (see the Computational Procedure section). In addition, LTNE formulations require specification as to how the heat flux at the bottom is shared among the solid and fluid phases. Equations (1*g*) and (1*h*) assume local thermal equilibrium at the wall and that the heat flux is distributed according to the effective thermal conductivity of each phase [51].

Consider the following dimensionless parameters:

$$\theta_f = k_f\frac{T_f - T_{\text{in}}}{q_{w,0}d} \tag{2a}$$

$$\theta_s = k_f\frac{T_s - T_{\text{in}}}{q_{w,0}d} \tag{2b}$$

$$\xi = \frac{x}{d\text{Pe}_d} \tag{2c}$$

$$\eta = \frac{y}{d} \tag{2d}$$

$$\tau = \frac{\alpha_f t}{d^2} \tag{2e}$$

$$\text{Pe}_d = \frac{ud}{\alpha_f} \tag{2f}$$

$$\text{Nu}_{fs} = \frac{h_{fs}(a_{fs}d^2)}{k_f} \tag{2g}$$

$$Q_w = \frac{q_w}{q_{w,0}} \tag{2h}$$

$$\Omega = \frac{\omega d^2}{\alpha_f} \tag{2i}$$

$$W_s = \frac{(\rho c_p)_s}{(\rho c_p)_f} \tag{2j}$$

$$K_s = \frac{k_s}{k_f} \tag{2k}$$

where ξ and η are the dimensionless horizontal and vertical coordinates, respectively, τ is the dimensionless time, θ_s and θ_f are the dimensionless temperatures of the solid and fluid phases, respectively, Pe_d is the Péclet number, Nu_{fs} is the interstitial Nusselt number, Q_w is the dimensionless heat flux, Ω is the dimensionless angular frequency of the heat flux, W_s is the ratio of the solid and fluid phases heat capacities, and K_s is the ratio of the solid and fluid phases thermal conductivities.

The dimensionless form of the model of Eqs. (1*a*) and (1*k*) then becomes

$$W_s(1-\varepsilon)\frac{\partial\theta_s}{\partial\tau} = K_s(1-\varepsilon)\left[\frac{1}{\mathrm{Pe}_d^2}\frac{\partial^2\theta_s}{\partial\xi^2} + \frac{\partial^2\theta_s}{\partial\eta^2}\right] - \mathrm{Nu}_{fs}(\theta_s - \theta_f) \tag{3a}$$

$$\varepsilon\frac{\partial\theta_f}{\partial\tau} + \frac{\partial\theta_f}{\partial\xi} = \varepsilon\left[\frac{1}{\mathrm{Pe}_d^2}\frac{\partial^2\theta_f}{\partial\xi^2} + \frac{\partial^2\theta_f}{\partial\eta^2}\right] - \mathrm{Nu}_{fs}(\theta_f - \theta_s) \tag{3b}$$

with boundary conditions and dimensionless heat flux given by

$$\theta_s(0,\eta,\tau) = \theta_f(0,\eta,\tau) = 0 \tag{3c,d}$$

$$\left|\frac{\partial\theta_f}{\partial\xi}\right|_{\xi\to\infty} < \infty \tag{3e}$$

$$\left|\frac{\partial\theta_s}{\partial\xi}\right|_{\xi\to\infty} < \infty \tag{3f}$$

$$\theta_f(\xi,0,\tau) = \theta_s(\xi,0,\tau) \tag{3g}$$

$$Q_w(\tau) = -K_s(1-\varepsilon)\left.\frac{\partial\theta_s}{\partial\eta}\right|_{\eta=0} - \varepsilon\left.\frac{\partial\theta_f}{\partial\eta}\right|_{\eta=0} \tag{3h}$$

$$\left.\frac{\partial\theta_f}{\partial\eta}\right|_{\eta=1} = \left.\frac{\partial\theta_s}{\partial\eta}\right|_{\eta=1} = 0 \tag{3i,j}$$

$$Q_w(\tau) = \cos(\Omega\tau) \tag{3k}$$

Filtering Procedure. Rather than analyzing an arbitrary unsteady physical situation, the present work deals with the periodic state characterized by the temperature fields in both the solid and fluid phases oscillating with the same frequency as the applied heat load [23,24]. In these circumstances, it is convenient to work with complex numbers and extract the behavior along the time variable into the exponential of $i\Omega\tau$, where $i = \sqrt{-1}$. To properly recover a real number when evaluating θ_s and θ_f, the following solution is proposed:

$$\theta_s(\xi,\eta,\tau) = \Re\left\{e^{i\Omega\tau}[F_s(\xi,\eta) + \Theta_s(\xi,\eta)]\right\} \tag{4a}$$

$$\theta_f(\xi,\eta,\tau) = \Re\left\{e^{i\Omega\tau}[F_f(\xi,\eta) + \Theta_f(\xi,\eta)]\right\} \tag{4b}$$

where $\Re$ means the real part of, F_s and F_f are real filter solutions for the solid and fluid phases, respectively, and Θ_s and Θ_f are, respectively, complex filtered dimensionless temperatures of the solid and fluid phases. Though not of interest in the present application, the imaginary part of the solution in Eqs. (4*a*) and (4*b*) leads to the periodic response of the dimensionless temperature to the sine functional form of the heat flux excitation, $Q_w(\tau) = \sin(\Omega\tau)$.

Ideally, the filter functions F_s and F_f should contain as much physical information as possible, enabling enhanced convergence of the solution using the GITT [32,52]. For this purpose, the steady-state thermally developed solutions of Eqs. (3*a*)–(3*k*) when $\Omega = 0$ are proposed as filters. Mathematically, the following set of equations are proposed for F_s and F_f:

$$0 = K_s(1-\varepsilon)\frac{\partial^2 F_s}{\partial\eta^2} - \mathrm{Nu}_{fs}(F_s - F_f) \tag{5a}$$

$$\frac{\partial F_f}{\partial\xi} = \varepsilon\frac{\partial^2 F_f}{\partial\eta^2} - \mathrm{Nu}_{fs}(F_f - F_s) \tag{5b}$$

with boundary conditions given by

$$F_f(\xi,0) = F_s(\xi,0) \tag{5c}$$

$$1 = -K_s(1-\varepsilon)\left.\frac{\partial F_s}{\partial\eta}\right|_{\eta=0} - \varepsilon\left.\frac{\partial F_f}{\partial\eta}\right|_{\eta=0} \tag{5d}$$

$$\left.\frac{\partial F_s}{\partial\eta}\right|_{\eta=1} = \left.\frac{\partial F_f}{\partial\eta}\right|_{\eta=0} = 0 \tag{5e,f}$$

where for a thermally developed solution, yields

$$\frac{dF_m}{d\xi} = \frac{dF_w}{d\xi} = \frac{\partial F_f}{\partial\xi} \tag{5g,h}$$

$$\frac{F_s - F_w}{F_m - F_w} = \phi_s(\eta) \tag{5i}$$

$$\frac{F_f - F_w}{F_m - F_w} = \phi_f(\eta) \tag{5j}$$

Equations (5*a*)–(5*j*) can be solved analytically. The expressions obtained, however, are omitted for the sake of brevity. Substituting θ_s and θ_f by $e^{i\Omega\tau}[F_s + \Theta_s]$ and $e^{i\Omega\tau}[F_f + \Theta_f]$ into Eqs. (3*a*)–(3*k*) and using Eqs. (5*a*)–(5*j*), yields

$$i\Omega W_s(1-\varepsilon)(F_s + \Theta_s) = K_s(1-\varepsilon)\left[\frac{1}{\mathrm{Pe}_d^2}\frac{\partial^2\Theta_s}{\partial\xi^2} + \frac{\partial^2\Theta_s}{\partial\eta^2}\right] - \mathrm{Nu}_{fs}(\Theta_s - \Theta_f) \tag{6a}$$

$$i\Omega\varepsilon(F_f + \Theta_f) + \frac{\partial\Theta_f}{\partial\xi} = \varepsilon\left[\frac{1}{\mathrm{Pe}_d^2}\frac{\partial^2\Theta_f}{\partial\xi^2} + \frac{\partial^2\Theta_f}{\partial\eta^2}\right] - \mathrm{Nu}_{fs}(\Theta_f - \Theta_s) \tag{6b}$$

with boundary conditions given by

$$\Theta_s(0,\eta) = -F_s(0,\eta) \tag{6c}$$

$$\Theta_f(0,\eta) = -F_f(0,\eta) \tag{6d}$$

$$\left|\frac{\partial\Theta_f}{\partial\xi}\right|_{\xi\to\infty} < \infty \tag{6e}$$

$$\left|\frac{\partial\Theta_s}{\partial\xi}\right|_{\xi\to\infty} < \infty \tag{6f}$$

$$\Theta_f(\xi,0) = \Theta_s(\xi,0) \tag{6g}$$

$$K_s(1-\varepsilon)\left.\frac{\partial\Theta_s}{\partial\eta}\right|_{\eta=0} + \varepsilon\left.\frac{\partial\Theta_f}{\partial\eta}\right|_{\eta=0} = 0 \tag{6h}$$

$$\left.\frac{\partial \Theta_f}{\partial \eta}\right|_{\eta=1} = \left.\frac{\partial \Theta_s}{\partial \eta}\right|_{\eta=1} = 0 \tag{6i,j}$$

Eigenvalue Problem. To solve Eqs. (6*a*)–(6*j*) using the GITT, an eigenvalue problem must be proposed, from which the basis for the eigenfunction expansion derives. The model is comprised of two partial differential equations and traditionally it would require that two independent Sturm–Liouville-type eigenvalue problems be proposed and solved, one for each of the unknown potentials Θ_s and Θ_f. The integral transform procedure would then provide two sets of coupled ordinary differential equations for the transformed potentials to be solved. This is a more cumbersome endeavor, and another path is taken in this work. Building upon previous contributions [13,33,49], the following coupled eigenvalue problem is proposed:

$$K_s(1-\varepsilon)\frac{d^2\psi_{s,m}}{d\eta^2} - \mathrm{Nu}_{fs}\left(\psi_{s,m} - \psi_{f,m}\right) = 0 \tag{7a}$$

$$\varepsilon\frac{d^2\psi_{f,m}}{d\eta^2} + \lambda_m^2\psi_{f,m} - \mathrm{Nu}_{fs}\left(\psi_{f,m} - \psi_{s,m}\right) = 0 \tag{7b}$$

with boundary conditions given by

$$\psi_{f,m}(0) = \psi_{s,m}(0) \tag{7c}$$

$$K_s(1-\varepsilon)\left.\frac{d\psi_{s,m}}{d\eta}\right|_{\eta=0} + \varepsilon\left.\frac{d\psi_{f,m}}{d\eta}\right|_{\eta=0} = 0 \tag{7d}$$

$$\left.\frac{d\psi_{f,m}}{d\eta}\right|_{\eta=1} = \left.\frac{d\psi_{s,m}}{d\eta}\right|_{\eta=1} = 0 \tag{7e,f}$$

and normalization given by

$$\tilde{\psi}_{s,m}(\eta) = \frac{\psi_{s,m}(\eta)}{\sqrt{N_m}} \tag{7g}$$

$$\tilde{\psi}_{f,m}(\eta) = \frac{\psi_{f,m}(\eta)}{\sqrt{N_m}} \tag{7h}$$

$$N_m = \int_0^1 \psi_{f,m}(\eta)^2 d\eta \tag{7i}$$

Equations (7*a*)–(7*i*) can be solved analytically, but, once more, the expressions are omitted to be more concise. The eigenfunctions in Eqs. (7*g*) and (7*h*) are orthonormal [33,49], i.e.,

$$\int_0^1 \tilde{\psi}_{f,m}(\eta)\tilde{\psi}_{f,n}(\eta)d\eta = \delta_{mn} \tag{8}$$

where δ_{mn} is Kronecker's delta.

In turn, the orthogonality property allows for transform and inverse formulae to be proposed as,

Transform

$$\overline{\Theta}_m(\xi) = \int_0^1 \tilde{\psi}_{f,m}(\eta)\Theta_f(\xi,\eta)d\eta \tag{9a}$$

Inverse formulae

$$\Theta_s(\xi,\eta) = \sum_{m=1}^{\infty}\overline{\Theta}_m(\xi)\tilde{\psi}_{s,m}(\eta) \tag{9b}$$

$$\Theta_f(\xi,\eta) = \sum_{m=1}^{\infty}\overline{\Theta}_m(\xi)\tilde{\psi}_{f,m}(\eta) \tag{9c}$$

The solution proposal of Eqs. (9*b*) and (9*c*) segregates all the information as to how the temperatures in the solid and fluid phases differ and are coupled together, encoded into the eigenvalue problem of Eqs. (7*a*)–(7*i*), from the variation of the temperature fields along the ξ coordinate, conveyed by the transformed potential, $\overline{\Theta}_m(\xi)$. This feature allows for effective handling of the coupled two-equation LTNE formulation that has favored the adoption of the simplified one-equation LTE model by many researchers [14–16]. More detailed information on why the solution of the coupled eigenvalue problem of Eqs. (7*a*)–(7*i*) forms a basis for the space of possible solutions for the temperature fields can be found elsewhere [33,49].

Alternatively, a more informative eigenvalue problem could have been adopted, by incorporating the left-hand sides of Eqs. (6*a*) and (6*b*), which carry the information on the periodic regimen, through the dimensionless oscillation frequency. However, as will be seen in what follows, it was sufficient and less cumbersome to consider this class IV problem defined in the real domain only, even if larger truncation orders are needed with the increase in the frequency.

Transformed Problem. Operating Eqs. (6*a*) and (6*b*), respectively, with $\int_0^1 \tilde{\psi}_{s,m}(\eta)(\cdot)d\eta$ and $\int_0^1 \tilde{\psi}_{f,m}(\eta)(\cdot)d\eta$, summing the resulting expressions, using the orthogonality property, substituting the inverse formulae of Eqs. (9*b*) and (9*c*), and rearranging, yields

$$\frac{1}{\mathrm{Pe}_d^2}\sum_{n=1}^{\infty}B_{mn}\frac{d^2\overline{\Theta}_n}{d\xi^2} = \frac{d\overline{\Theta}_m}{d\xi} + \sum_{n=1}^{\infty}D_{mn}\overline{\Theta}_n + i\Omega\left(\overline{g}_m + \overline{h}_m\xi\right), \quad m = 1,2,\ldots \tag{10a}$$

with boundary conditions, obtained by applying $\int_0^1 \tilde{\psi}_{f,m}(\eta)(\cdot)d\eta$ to Eqs. (6*d*) and (6*e*), given by

$$\overline{\Theta}_m(0) = \overline{f}_m \tag{10b}$$

$$\left|\frac{d\overline{\Theta}_m}{d\xi}\right|_{\xi\to\infty} < \infty \tag{10c}$$

and integral coefficients

$$B_{mn} = K_s(1-\varepsilon)\int_0^1 \tilde{\psi}_{s,m}(\eta)\tilde{\psi}_{s,n}(\eta)d\eta + \varepsilon\delta_{mn} \tag{10d}$$

$$C_{mn} = W_s(1-\varepsilon)\int_0^1 \tilde{\psi}_{s,m}(\eta)\tilde{\psi}_{s,n}(\eta)d\eta + \varepsilon\delta_{mn} \tag{10e}$$

$$D_{mn} = \lambda_m^2\delta_{mn} + i\Omega C_{mn} \tag{10f}$$

$$\overline{f}_m = -\int_0^1 \tilde{\psi}_{f,m}(\eta)F_f(0,\eta)d\eta \tag{10g}$$

$$\overline{g}_m = W_s(1-\varepsilon)\int_0^1 \tilde{\psi}_{s,m}(\eta)F_s(0,\eta)d\eta - \varepsilon\overline{f}_m \tag{10h}$$

$$\overline{h}_m = W_s(1-\varepsilon)\int_0^1 \tilde{\psi}_{s,m}(\eta)d\eta + \varepsilon\int_0^1 \tilde{\psi}_{f,m}(\eta)d\eta \tag{10i}$$

Computational Procedure. The system of ordinary differential equations (10*a*)–(10*i*) must be truncated to a finite order so it can be handled computationally, which is accomplished by carrying out the sums in the inverse formulae of Eqs. (9*b*) and (9*c*) up to $\mathcal{N}$ terms. As a result, the truncated system is comprised of $\mathcal{N}$

ordinary differential equations and each summation within them retains up to $\mathcal{N}$ terms.

The truncated system can be handled analytically. For this purpose, it must be rewritten as a system of first-order differential equations by defining

$$X_m(\xi) = \overline{\Theta}_m(\xi), \quad m = 1, 2, \ldots, \mathcal{N} \tag{11a}$$

$$X_{\mathcal{N}+m}(\xi) = \frac{d\overline{\Theta}_m}{d\xi}, \quad m = 1, 2, \ldots, \mathcal{N} \tag{11b}$$

$$\mathbf{X}(\xi) = \{X_r(\xi)\}_{r=1,2,\ldots,2\mathcal{N}} \tag{11c}$$

The definitions of Eqs. (11*a*)–(11*c*) allow for the truncated transformed problem to be rewritten as

$$\frac{d\mathbf{X}}{d\xi} = MX(\xi) + a + b\xi \tag{12a}$$

with coefficients matrix and source vector

$$M = \begin{bmatrix} 0 & \mathbf{I} \\ \mathrm{Pe}_d^2\mathbf{B}^{-1}\mathbf{D} & \mathrm{Pe}_d^2\mathbf{B}^{-1} \end{bmatrix} \tag{12b}$$

$$a = \mathrm{Pe}_d^2\mathbf{B}^{-1}\overline{\mathbf{g}} \tag{12c}$$

$$b = \mathrm{Pe}_d^2\mathbf{B}^{-1}\overline{\mathbf{h}} \tag{12d}$$

where $\mathbf{B} = \{B_{mn}\}_{m,n=1,2,\ldots,\mathcal{N}}$, $\mathbf{D} = \{D_{mn}\}_{m,n=1,2,\ldots,\mathcal{N}}$, $\mathbf{I} = \{\delta_{mn}\}_{m,n=1,2,\ldots,\mathcal{N}}$, $\overline{\mathbf{g}} = \{\overline{g}_m\}_{m=1,2,\ldots,\mathcal{N}}$, and $\overline{\mathbf{h}} = \{\overline{h}_m\}_{m=1,2,\ldots,\mathcal{N}}$.

Equations (12*a*)–(12*c*) can be diagonalized with the help of the eigenvectors of the matrix $\mathbf{M}$ computed using the *Eigensystem* function of the *Wolfram Mathematica v13.0* platform [50,53]. Let $\mathbf{\Phi}$ be a matrix whose columns are the eigenvectors of $\mathbf{M}$ and $\mathbf{X} = \mathbf{\Phi\varphi}$. Then, Eqs. (12*a*)–(12*c*) can be rewritten as

$$\frac{d\boldsymbol{\varphi}}{d\xi} = \mathbf{\Lambda\varphi} + \hat{\mathbf{a}} + \hat{\mathbf{b}}\xi \tag{13}$$

where $\Lambda = \{\zeta_r\delta_{rs}\}_{r=1,2,\ldots,2\mathcal{N}}$ is a matrix with the eigenvalues of $\mathbf{M}$, ζ_r (also obtained with the eigensystem routine [50]), in its diagonal and whose other elements are zero, $\hat{\mathbf{a}} = \mathbf{\Phi}^{-1}\mathbf{a} = \{\hat{a}_r\}_{r=1,2,\ldots,2\mathcal{N}}$, $\hat{\mathbf{b}} = \mathbf{\Phi}^{-1}\mathbf{b} = \{\hat{b}_r\}_{r=1,2,\ldots,2\mathcal{N}}$, and $\boldsymbol{\varphi} = \{\varphi_r\}_{r=1,2,\ldots,2\mathcal{N}}$. Equation (13) can be solved analytically in the form

$$\varphi_r(\xi) = c_r\exp(\zeta_r\xi) - \frac{\hat{a}_r}{\zeta_r} - \frac{\hat{b}_r}{\zeta_r}\left(\xi + \frac{1}{\zeta_r}\right) \tag{14}$$

To avoid an unrealistic exponential growth in both $|\Theta_s|$ and $|\Theta_f|$ along ξ, c_r is set to zero for all values of r where $\Re\{\zeta_r\} > 0$, which corresponds to half the values in $\{\zeta_r\}_{r=1,2,\ldots,2\mathcal{N}}$. The practical consequence is the bounded temperature derivatives of the boundary conditions (1*e*) and (1*f*) and (6*e*) and (6*f*).

The vector $\mathbf{X}$ is then recovered as follows:

$$\mathbf{X}(\xi) = \mathbf{\Phi\varphi}(\xi) \tag{15}$$

Finally, the entry condition of Eq. (10*b*) is enforced upon the first $\mathcal{N}$ elements of $\mathbf{X}$, yielding a linear system to be solved for the remaining coefficients c_r. This linear system is solved with the function LinearSolve of the Wolfram Mathematica v13.0 platform [50], completing the solution of the transformed problem.

Once the transformed problem is solved, the inverse formulae of Eqs. (9*b*) and (9*c*) are used to recover the potentials Θ_s and Θ_f. Some relevant results can then be extracted from these potentials. Their sum with the filters, F_s and F_f, are complex numbers, and their absolute values and complex arguments are the amplitudes and phase shifts of the dimensionless temperature fields, respectively. These quantities can be calculated using the functions Abs and Arg of the Wolfram Mathematica v13.0 platform [50]. The thermal lags for the solid and fluid phases in a particular position along the porous channel are then obtained by, respectively, dividing the complex arguments of Θ_s and Θ_f by the angular frequency, Ω.

Lastly, the dimensionless temperature fields are retrieved using Eqs. (4*a*) and (4*b*). The temperature at the bottom wall can then be evaluated as

$$\theta_w(\xi, \tau) = \theta_s(\xi, 0, \tau) = \theta_f(\xi, 0, \tau) \tag{16a,b}$$

where θ_w is the dimensionless temperature at the bottom wall.

Results and Discussion

Base Case. A base case, stemming from a microchannel-based thermal device made of plexiglass through which flows air, is chosen to illustrate the solution method. The thermal device is comprised of 25 microchannels 200 μm wide, 1 mm tall, and 10 mm long. The air flowrate is 10 L/min. Using the upscaling model proposed in Ref. [13], the dimensionless entry parameters shown in Table 1 are obtained.

Convergence Analysis. Before analyzing the periodic response and overall behavior of the porous channel, the convergence of the results must be checked. Let $F_s + \Theta_s$ and $F_f + \Theta_f$ be written as $\mathcal{A}_s e^{i\Omega\beta_s}$ and $\mathcal{A}_f e^{i\Omega\beta_f}$, respectively, where $\mathcal{A}_s$ and $\mathcal{A}_f$ are the amplitudes of oscillation in the temperature fields for the solid and fluid, whereas β_s and β_f are the thermal lags for these same phases. Defining

$$\epsilon_{\mathcal{A}}(\mathcal{N}) = \left|\frac{\mathcal{A}|_{\mathcal{N}=200} - \mathcal{A}|_{\mathcal{N}}}{\mathcal{A}|_{\mathcal{N}=200}}\right| \tag{17a}$$

$$\epsilon_{\beta}(\mathcal{N}) = \left|\frac{\beta|_{\mathcal{N}=200} - \beta|_{\mathcal{N}}}{\beta|_{\mathcal{N}=200}}\right| \tag{17b}$$

where $\epsilon_{\mathcal{A}}$ and ϵ_{β} are the truncation errors for the amplitude and thermal lag as compared to their values at $\mathcal{N} = 200$. Figures 2(*a*) and 3(*a*) present the truncation errors of the amplitude in the temperature fields for the solid and fluid phases, respectively, as a function of the truncation order, $\mathcal{N}$. These results are for the base case. It is clear from these graphs that the convergence of the solid temperature is much smoother. Similar conclusions are reached by analyzing Figs. 2(*b*) and 3(*b*) with a noticeable slower convergence of the thermal lag at $\eta = 0.25$.

Table 2 presents more detailed information regarding the convergence of the thermal lag in the fluid and solid temperature fields. As imposed by the boundary condition of Eq. (6*g*), the thermal lag at the bottom wall ($\eta = 0$) is the same for the solid and fluid phases. Increasing the truncation order from $\mathcal{N} = 195$ to $\mathcal{N} = 200$ changes the obtained thermal lag by at most 0.26%,

Table 1 Dimensionless parameters for the base case

Variable name	Symbol	Value
Porosity	ε	0.5
Péclet number	Pe_d	767
Interstitial Nusselt number	Nu_{fs}	111
Dimensionless angular frequency	Ω	1
Ratio of thermal capacities	W_s	1475
Ratio of thermal conductivities	K_s	7.39

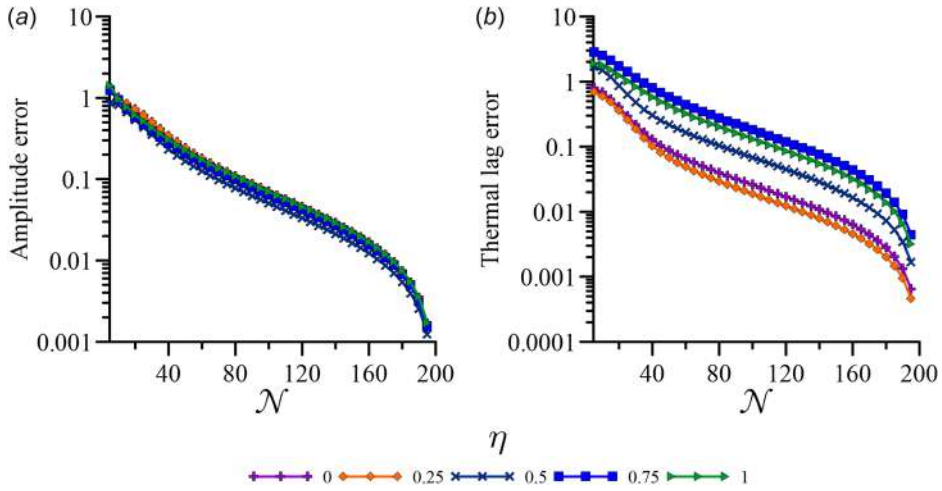

Fig. 2 Truncation errors of the amplitude and thermal lag of the solid dimensionless temperature: (*a*) amplitude of the temperature oscillation and (*b*) thermal lag

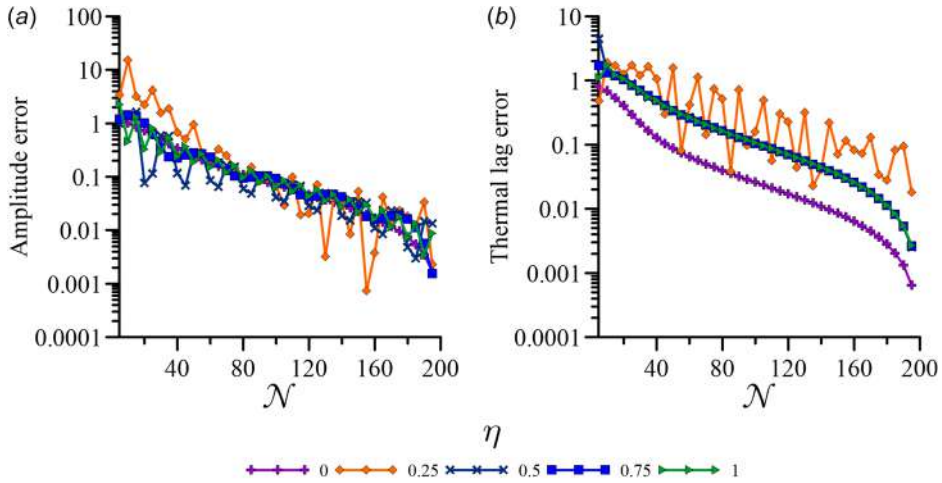

Fig. 3 Truncation errors of the amplitude and thermal lag of the fluid dimensionless temperature: (*a*) amplitude of the temperature oscillation and (*b*) thermal lag

Table 2 Convergence of the thermal lag of the fluid and solid phases temperature fields (data from base case)

	Solid			Fluid		
$\mathcal{N}$	$\eta = 0$	$\eta = 0.25$	$\eta = 0.5$	$\eta = 0$	$\eta = 0.25$	$\eta = 0.5$
50	−1.0071	−0.9547	−0.3181	−1.0071	−1.8005	0.6732
100	−1.0750	−1.0039	−0.3786	−1.0750	−0.8161	0.5582
120	−1.0847	−1.0106	−0.3880	−1.0847	−0.8627	0.5397
140	−1.0916	−1.0152	−0.3946	−1.0916	−0.7321	0.5269
160	−1.0966	−1.0185	−0.3994	−1.0966	−0.7614	0.5175
170	−1.0987	−1.0199	−0.4014	−1.0987	−0.7958	0.5136
180	−1.1005	−1.0211	−0.4032	−1.1005	−0.6841	0.5103
190	−1.1021	−1.0222	−0.4047	−1.1021	−0.6375	0.5073
195	−1.1029	−1.0227	−0.4054	−1.1029	−0.7163	0.5059
200	−1.1036	−1.0232	−0.4061	−1.1036	−0.7037	0.5046
Relative difference	0.06%	0.05%	0.17%	0.06%	1.76%	0.26%

except for the fluid at $\eta = 0.25$, which was already identified as slowly converging in Fig. 3(*b*), where the change of the thermal lag reaches 1.76%. Nevertheless, these results are satisfactory in the envisioned applications and $\mathcal{N} = 200$ is henceforth employed throughout.

Verification and Validation. To build further confidence on the results to follow, a verification and validation effort are carried out by comparing, respectively, with numerical [13] and experimental [54] results available in the literature. The results of these comparisons are depicted in Fig. 4. In this graph, the dependency

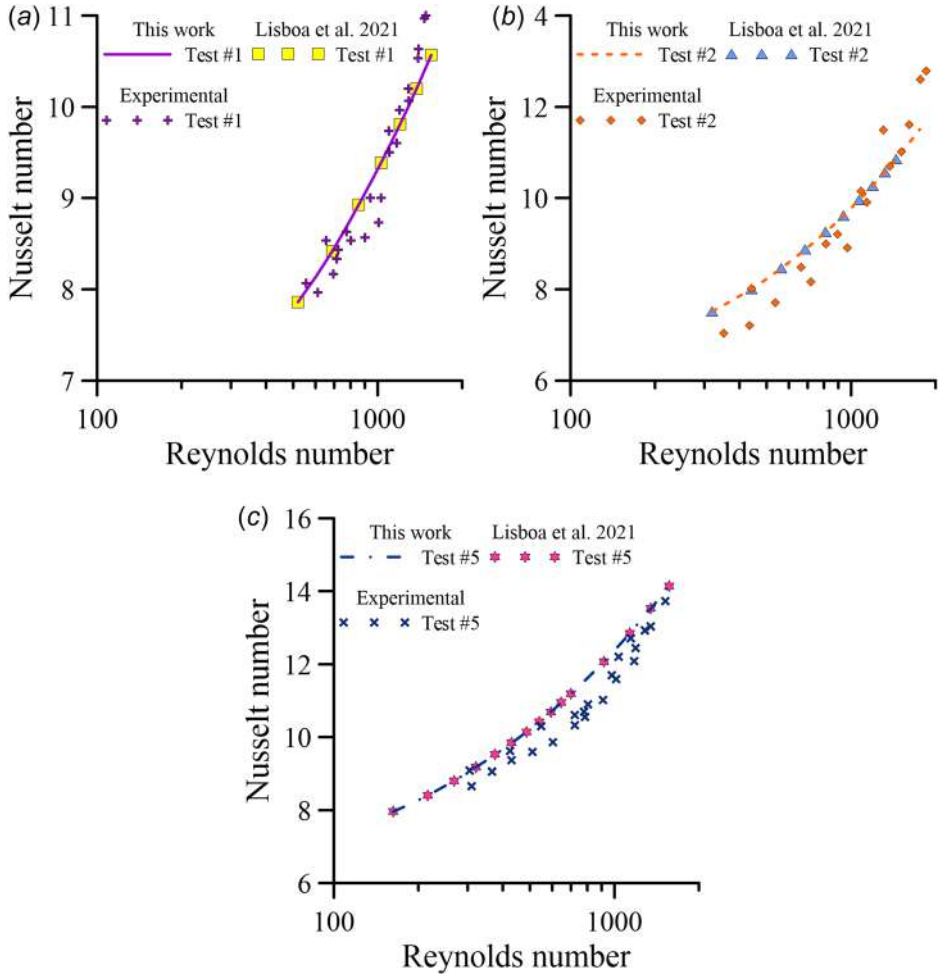

Fig. 4 Comparison of the behavior of the Nusselt number for varying Reynolds number against numerical [13] and experimental [54] results from the literature: (*a*) test #1, (*b*) test #2, and (*c*) test #5

Table 3 Parameters of the experimental cases used in the validation [54]

		Values		
Variable name	Symbol	Test #1	Test #2	Test #5
Number of microchannels	—		10	
Width of the microchannels (μm)	—	194	229	534
Height of the microchannels (μm)	—	884	1250	2910
Ratio of thermal capacities	W_s		0.82589	
Ratio of thermal conductivities	K_s		654.65	

of the Nusselt number on the Reynolds number for three test cases involving water flow through rectangular microchannels machined in a copper block. Some relevant parameters for each test case are presented in Table 3 and more information on the definitions of the Nusselt and Reynolds numbers can be found elsewhere [54]. Both numerical and experimental results are for steady-state, then the results from the curves in Fig. 4 were obtained by setting $\Omega = 0$.

The agreement of the results from this work with the experimental ones is good, with a somewhat more pronounced deviation for test case #5, however, it is here presumed to be within experimental errors, even though the authors of that work did not provide a thorough uncertainty analysis [54]. Adherence to the numerical results from the literature is perfect to the graph scale, and considering that the methodology of that work was evaluated against experimental results for other independent experimental results involving metal foams and pin fins heat sinks [13], it further corroborates the adequacy of the present methodology and of the associated computational code.

Physical Analysis. Figures 5(*a*) and 5(*b*) present contour plots for the thermal lag of the fluid and solid phases in the base case, respectively. Positive values for the thermal lag mean that, at that point, the temperature is at least half period behind the periodic heat load; this fact is due to output of the Arg function being defined in the interval $[-\pi, \pi]$ [50]. As expected, for both the solid and fluid phases, the thermal lag is more pronounced in regions relatively close to the bottom wall, but not at it. The reason for this behavior is that the information of the heat flux imposed at the wall was not yet able to reach these intermediate layers, while layers farther away from the wall are still experiencing the heat front produced by the prior cycle and thus present milder phase shifts. In addition, the thermal lag seems to be more pronounced in the fluid than in the solid.

To get a clearer picture of what was discussed in the previous paragraph, Figs. 6(*a*) and 6(*b*) present dimensionless temperature profiles, respectively, for the fluid and solid phases at $\xi = 0.03$ (roughly equivalent to 10 mm from the inlet) for four times within a period of oscillation of the heat flux. Indeed, the thermal lag is shown to be more prominent for the fluid phase. At $\Omega\tau/2\pi = 0.25$ ends a heating process, while at $\Omega\tau/2\pi = 0.75$ a cooling process is terminated. Nonetheless, the fluid at $\eta \cong 0.1$ is colder than the wall at $\Omega\tau/2\pi = 0.25$ and hotter than the wall at $\Omega\tau/2\pi = 0.75$,

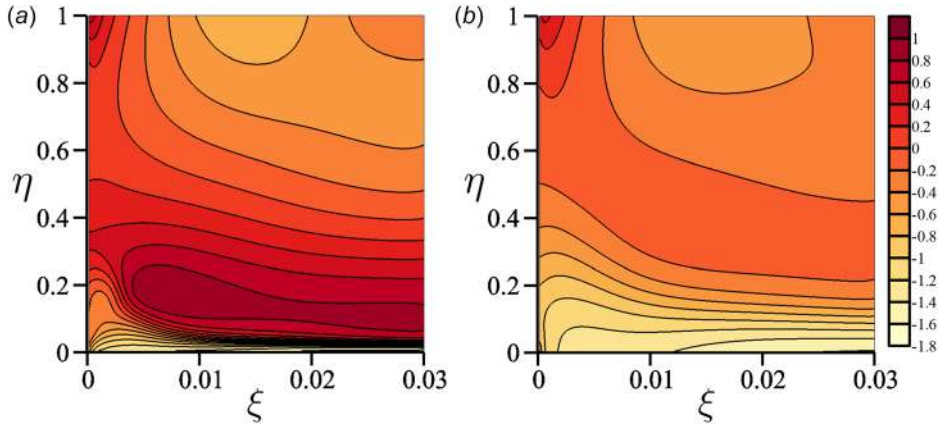

Fig. 5 Contours of thermal lag along the porous channel: (*a*) fluid phase and (*b*) solid phase. The scale bar is valid for both graphs.

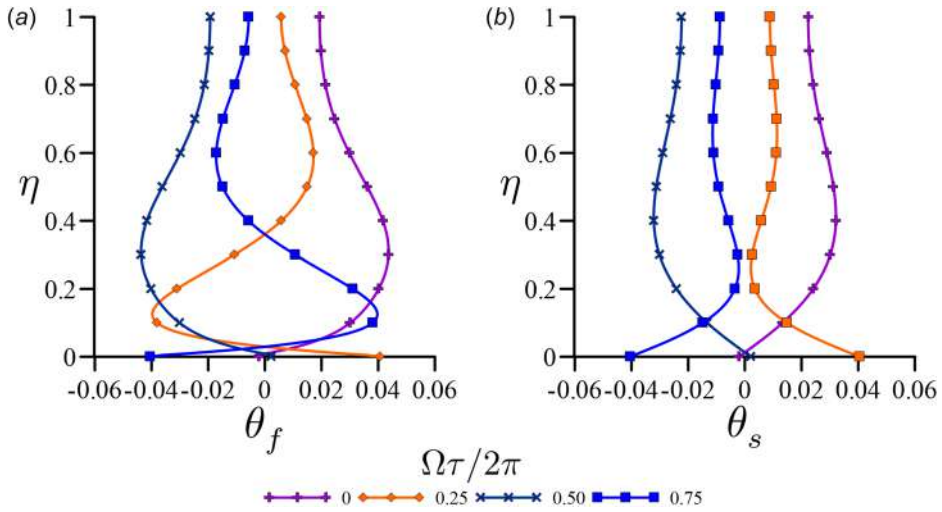

Fig. 6 Dimensionless temperature profiles for four equally spaced times within a period of oscillation of the heat load: (*a*) fluid phase and (*b*) solid phase

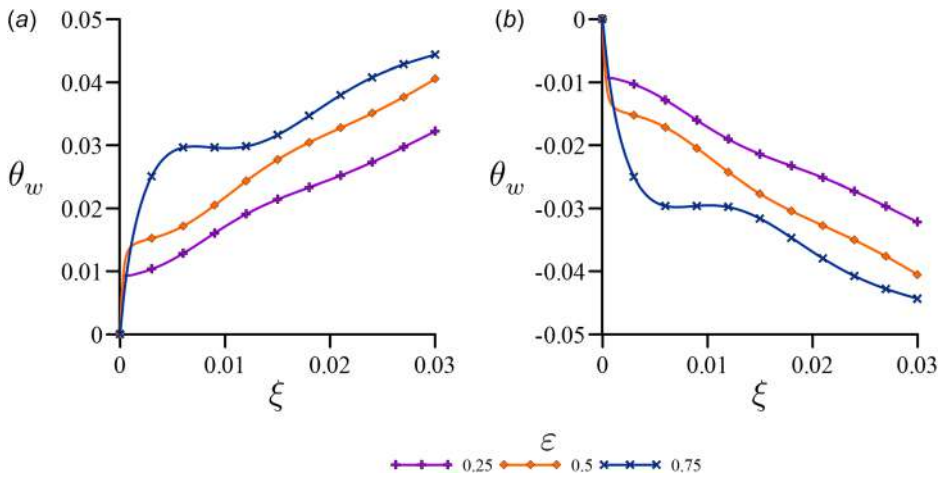

Fig. 7 Dimensionless wall temperature along the horizontal coordinate for three values of the porosity of the porous channel: (*a*) $\tau = 0.25$ and (*b*) $\tau = 0.75$

which is indicative of the thermal lag. This behavior is also present in the solid, but at a much smaller degree. It is noteworthy that the temperature profiles for both phases differ significantly. Thus, the common adoption of the LTE hypothesis [14–16] may be inaccurate in periodic problems, where differences in thermal capacities and the related thermal lag can introduce large temperature differences, thus confirming the necessity of adopting the LTNE hypothesis in such unsteady situations.

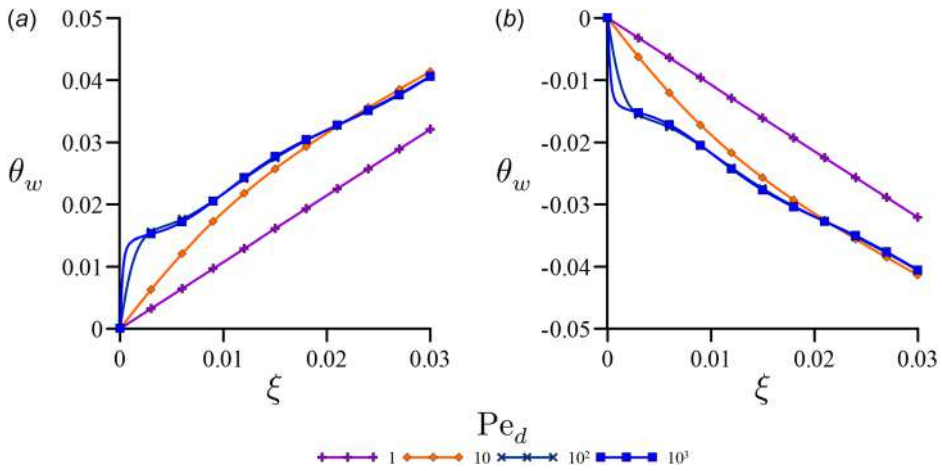

Fig. 8 Dimensionless wall temperature along the horizontal coordinate for four values of the Péclet number: (*a*) $\tau = 0.25$ and (*b*) $\tau = 0.75$

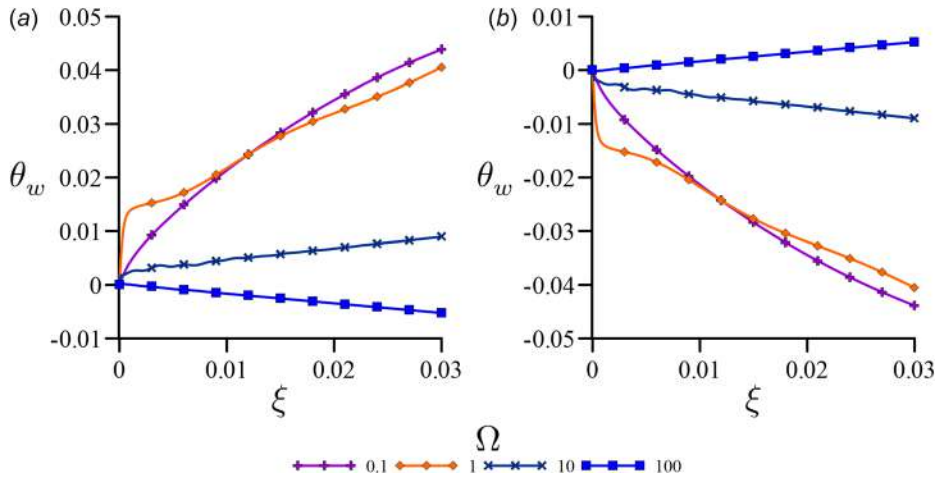

Fig. 9 Dimensionless wall temperature along the horizontal coordinate for four values of the angular frequency: (*a*) $\tau = 0.25$ and (*b*) $\tau = 0.75$

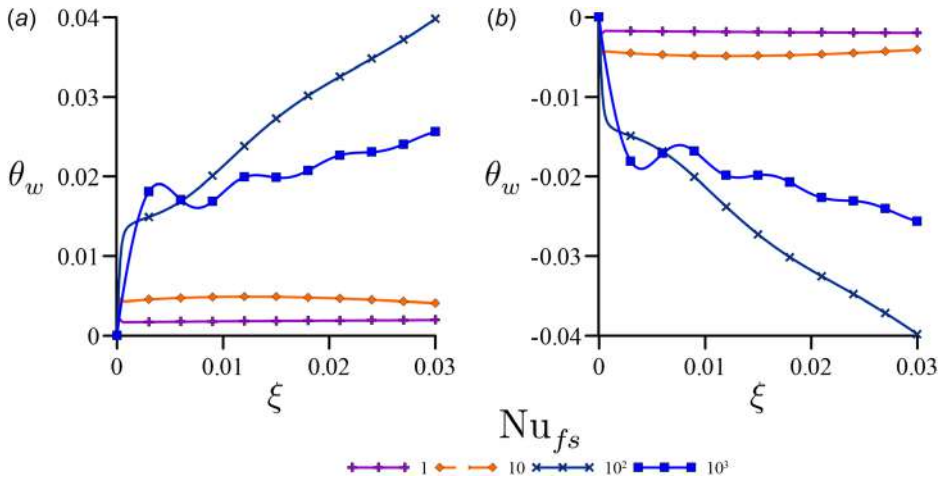

Fig. 10 Dimensionless wall temperature along the horizontal coordinate for four values of the interstitial Nusselt number: (*a*) $\tau = 0.25$ and (*b*) $\tau = 0.75$

Figures 7–10 present the wall temperature at two instants of time, namely, $\Omega\tau/2\pi = 0.25$ and $\Omega\tau/2\pi = 0.75$, for varying dimensionless parameters such as ε, Nu_{fs}, Ω, and Pe_d. At the end of the heating process, i.e., $\Omega\tau/2\pi = 0.25$, if thermal lag was zero, the wall temperature should be considerably above the inlet temperature and $\theta_w > 0$. On the other hand, at the end of the cooling process ($\Omega\tau/2\pi = 0.75$), the opposite should occur. Thus, the higher θ_w at $\Omega\tau/2\pi = 0.25$ and the lower θ_w at $\Omega\tau/2\pi = 0.75$, the

lower the thermal lag. As a result, higher porosities, ε, and Péclet numbers, Pe_d, and lower angular frequencies, Ω, lead to smaller thermal lags. The dependency on the interstitial Nusselt number, however, is not monotonic, with increases in Nu_{fs} mostly disfavoring thermal lag up until $\mathrm{Nu}_{fs} \cong 10^2$, from which point the thermal lag begins to increase. Overall, the more of the channel is occupied by the solid phase and the worse the heat transfer rate between phases, more pronounced the thermal lag will be. In fact, the solid appears to function as an accumulator of thermal energy exacerbating the thermal lag.

Interestingly, a wavelike behavior along ξ is apparent as Pe_d grows, as seen in Fig. 8. Analyzing the transformed problem of Eqs. (10*a*)–(10*i*) truncated at $\mathcal{N} = 1$, as $\mathrm{Pe}_d \to \infty$, a term proportional to $\exp(-i\Omega C_{11}\xi)$ in the resulting expression for $\overline{\Theta}_1$ appears and it is responsible for the observed oscillatory behavior. For low values of Pe_d, if an adiabatic porous channel section before the entrance at $\xi = 0$, the results of this work may prove inaccurate due to backpropagation of thermal energy upstream, as described in Ref. [55].

Conclusions

An integral transform solution of the thermal transport in a microdevice subjected to a periodic heat load, reformulated as a porous medium with upscaled models representing microscale features, was presented. First, the periodic problem is reformulated as a quasi-steady problem by extracting the oscillatory information into new terms with complex numbers in place of the time derivative operator. Moreover, the employment of a coupled eigenvalue problem allowed for the attainment of a single set of ordinary differential equations encompassing solid and fluid heat transfer phenomena when the LTNE formulation is adopted, with little added computational effort compared to the adoption of the LTE hypothesis, which is shown to be inadequate in the present class of problems.

The model and computational code were verified and validated against previously published numerical and experimental results with good agreement. Finally, thermal lag was shown to be deeply affected by some key dimensionless parameters, such as Péclet and interstitial Nusselt numbers, porosity, and dimensionless angular frequency. In sum, microdevices with larger portions occupied by the solid phase tend to introduce more thermal inertia and induce larger thermal lags, at least for the situation here analyzed. Furthermore, poorer heat transfer contributes to increased thermal lag.

Acknowledgment

This work is dedicated to Professor Ivan Catton, for his dedication to the advancement of thermal sciences through his numerous pioneering works and the many researchers prepared under his guidance. RMC is particularly honored for having his friendship and continuous support throughout the academic career.

Funding Data

- Conselho Nacional de-Desenvolvimento Científico e Tecnológico (CNPq) (Funder ID: 10.13039/501100003593).
- Coordenação de-Aperfeiçoamento de-Pessoal de-Nível Superior (CAPES) (Funder ID: 10.13039/501100002322).
- Fundação Carlos Chagas Filho de-Amparo à Pesquisa do Estado do Rio de-Janeiro (FAPERJ) (Grant Nos. E-26/010/002590/2019 and E-26/211.519/2021; Funder ID: 10.13039/501100004586).

Data Availability Statement

The datasets generated and supporting the findings of this article are obtainable from the corresponding author upon reasonable request.

Nomenclature

$\mathcal{A}$ = amplitude of oscillation in the temperature field
a_{fs} = specific surface area of the porous medium
B, C, D = integral coefficients with two indices
c_p = specific heat at constant temperature
d = height of the porous medium
F = filter solution
$\overline{f}, \overline{g}, \overline{h}$ = integral coefficients with one index
h_{fs} = interstitial heat transfer coefficient
k = thermal conductivity
K_s = ratio of the solid and fluid thermal conductivities
N_m = norm
Nu_{fs} = interstitial Nusselt number
Pe_d = Péclet number
q_w = heat flux
$q_{w,0}$ = heat flux amplitude
Q_w = dimensionless heat flux
t = time
T = temperature
u = seepage velocity of the fluid in the porous medium
W_s = ratio of the solid and fluid phases heat capacities
x, y = Cartesian coordinates

Greek Symbols

α = thermal diffusivity
β = phase shift of the oscillation in the temperature field
δ_{mn} = Kronecker's delta
ϵ = truncation error
ε = porosity
η = dimensionless vertical coordinate
θ = dimensionless temperature
Θ = filtered dimensionless temperature
λ = eigenvalues
ξ = dimensionless horizontal coordinate
ρ = density
τ = dimensionless time
ψ = eigenfunctions
ω = angular frequency of the heat flux
Ω = dimensionless angular frequency of the heat flux

Superscripts and Subscripts

f = refers to the fluid phase
in = refers to the inlet
m, n = indices of the eigenfunction
s = refers to the solid phase
w = refers to the wall
$\overline{\cdot}$ = transformed quantity
$\sim$ = normalized quantity

References

[1] Kandlikar, S. G., Garimella, S., Li, D., Colin, S., and King, M. R., 2006, *Heat Transfer and Fluid Flow in Minichannels and Microchannels*, Elsevier, Oxford, UK.
[2] Tuckerman, D. B., and Pease, R. F. W., 1981, "High-Performance Heat Sinking for VLSI," IEEE Electron Device Lett., **2**(5), pp. 126–129.
[3] Sharma, C. S., Tiwari, M. K., Zimmermann, S., Brunschwiler, T., Schlottig, G., Michel, B., and Poulikakos, D., 2015, "Energy Efficient Hotspot-Targeted Embedded Liquid Cooling of Electronics," Appl. Energy, **138**, pp. 414–422.
[4] Royne, A., Dey, C. J., and Mills, D. R., 2005, "Cooling of Photovoltaic Cells Under Concentrated Illumination: A Critical Review," Sol. Energy Mater. Sol. Cells, **86**(4), pp. 451–483.
[5] Zimmermann, S., Meijer, I., Tiwari, M. K., Paredes, S., Michel, B., and Poulikakos, D., 2012, "Aquasar: A Hot Water Cooled Data Center With Direct Energy Reuse," Energy, **43**(1), pp. 237–245.
[6] Yakomaskin, A. A., Afanasiev, V. N., Zubkov, N. N., and Morskoy, D. N., 2013, "Investigation of Heat Transfer in Evaporator of Microchannel Loop Heat Pipe," ASME J. Heat Transfer, **135**(10), p. 101006.
[7] Nagayama, G., Gyotoku, S., and Tsuruta, T., 2018, "Thermal Performance of Flat Micro Heat Pipe With Converging Microchannels," Int. J. Heat Mass Transfer, **122**, pp. 375–382.
[8] Horvat, A., and Catton, I., 2003, "Numerical Technique for Modeling Conjugate Heat Transfer in an Electronic Device Heat Sink," Int. J. Heat Mass Transfer, **46**(12), pp. 2155–2168.
[9] Sbutega, K., and Catton, I., 2013, "Efficient Hydraulic and Thermal Analysis of Heat Sinks Using Volume Averaging Theory and Galerkin Methods," Multiphase Sci. Technol., **25**(2–4), pp. 311–338.

[10] Sbutega, K., and Catton, I., 2013, "Application of Fourier-Galerkin Method to Volume Averaging Theory Based Model of Heat Sinks," ASME Paper No. IMECE2013-65244.
[11] Sbutega, K., and Catton, I., 2016, "Galerkin Method Solution of a Volume-Averaged Model for Efficient Conjugate Heat Transfer Analysis," Numer. Heat Transfer, Part B, **69**(1), pp. 1–25.
[12] Bejan, A., 2004, "Designed Porous Media: Maximal Heat Transfer Density at Decreasing Length Scales," Int. J. Heat Mass Transfer, **47**(14–16), pp. 3073–3083.
[13] Lisboa, K. M., Zotin, J. L. Z., Naveira-Cotta, C. P., and Cotta, R. M., 2021, "Leveraging the Entropy Generation Minimization and Designed Porous Media for the Optimization of Heat Sinks Employed in Low-Grade Waste Heat Harvesting," Int. J. Heat Mass Transfer, **181**, p. 121850.
[14] Kaviany, M., 1985, "Laminar Flow Through a Porous Channel Bounded by Isothermal Parallel Plates," Int. J. Heat Mass Transfer, **28**(4), pp. 851–858.
[15] Poulikakos, D., and Renken, K., 1987, "Forced Convection in a Channel Filled With Porous Medium, Including the Effects of Flow Inertia, Variable Porosity, and Brinkman Friction," ASME J. Heat Transfer, **109**(4), pp. 880–888.
[16] Vafai, K., and Kim, S. J., 1989, "Forced Convection in a Channel Filled With a Porous Medium: An Exact Solution," ASME J. Heat Transfer, **111**(4), pp. 1103–1106.
[17] Quintard, M., Kaviany, M., and Whitaker, S., 1997, "Two-Medium Treatment of Heat Transfer in Porous Media: Numerical Results for Effective Properties," Adv. Water Resour., **20**(2–3), pp. 77–94.
[18] Nield, D. A., 1998, "Effects of Local Thermal Nonequilibrium in Steady Convective Processes in a Saturated Porous Medium: Forced Convection in a Channel," J. Porous Media, **1**, pp. 181–186.
[19] Nield, D. A., and Kuznetsov, A. V., 1999, "Local Thermal Nonequilibrium Effects in Forced Convection in a Porous Medium Channel: A Conjugate Problem," Int. J. Heat Mass Transfer, **42**(17), pp. 3245–3252.
[20] Vadasz, P., 2005, "Explicit Conditions for Local Thermal Equilibrium in Porous Media Heat Conduction," Transp. Porous Media, **59**(3), pp. 341–355.
[21] Mahmoudi, Y., and Karimi, N., 2014, "Numerical Investigation of Heat Transfer Enhancement in a Pipe Partially Filled With a Porous Material Under Local Thermal Non-Equilibrium Condition," Int. J. Heat Mass Transfer, **68**, pp. 161–173.
[22] Mahmoudi, Y., Karimi, N., and Mazaheri, K., 2014, "Analytical Investigation of Heat Transfer Enhancement in a Channel Partially Filled With a Porous Material Under Local Thermal Non-Equilibrium Condition: Effects of Different Thermal Boundary Conditions at the Porous-Fluid Interface," Int. J. Heat Mass Transfer, **70**, pp. 875–891.
[23] Kakaç, S., Li, W., and Cotta, R. M., 1990, "Unsteady Laminar Forced Convection in Ducts With Periodic Variation of Inlet Temperature," ASME J. Heat Transfer, **112**(4), pp. 913–920.
[24] Cheroto, S., Mikhailov, M. D., Kakaç, S., and Cotta, R. M., 1999, "Periodic Laminar Forced Convection: Solution Via Symbolic Computation and Integral Transforms," Int. J. Therm. Sci., **38**(7), pp. 613–621.
[25] Kośny, J., Biswas, K., Miller, W., and Kriner, S., 2012, "Field Thermal Performance of Naturally Ventilated Solar Roof With PCM Heat Sink," Sol. Energy, **86**(9), pp. 2504–2514.
[26] Jim, C. Y., 2014, "Heat-Sink Effect and Indoor Warming Imposed by Tropical Extensive Green Roof," Ecol. Eng., **62**, pp. 1–12.
[27] Onda, K., Ohshima, T., Nakayama, M., Fukuda, K., and Araki, T., 2006, "Thermal Behavior of Small Lithium-Ion Battery During Rapid Charge and Discharge Cycles," J. Power Sources, **158**(1), pp. 535–542.
[28] Kim, J., Oh, J., and Lee, H., 2019, "Review on Battery Thermal Management System for Electric Vehicles," Appl. Therm. Eng., **149**, pp. 192–212.
[29] Bernardo, L. R., Perers, B., Håkansson, H., and Karlsson, B., 2011, "Performance Evaluation of Low Concentrating Photovoltaic/Thermal Systems: A Case Study From Sweden," Sol. Energy, **85**(7), pp. 1499–1510.
[30] Muthu, G., Shanmugam, S., and Veerappan, A. R., 2014, "Solar Parabolic Dish Thermoelectric Generator With Acrylic Cover," Energy Procedia, **54**, pp. 2–10.
[31] Cotta, R. M., 1990, "Hybrid Numerical-Analytical Approach to Nonlinear Diffusion Problems," Numer. Heat Transfer, Part B, **17**(2), pp. 217–226.
[32] Cotta, R. M., 1993, *Integral Transforms in Computational Heat and Fluid Flow*, CRC Press, Boca Raton, FL.
[33] Mikhailov, M. D., and Ozisik, M. N., 1984, *Unified Analysis and Solutions of Heat and Mass Diffusion*, Wiley, New York.
[34] Aperecido, J. B., Cotta, R. M., and Özişik, M. N., 1989, "Analytical Solutions to Two-Dimensional Diffusion Type Problems in Irregular Geometries," J. Franklin Inst., **326**(3), pp. 421–434.
[35] Sphaier, L. A., and Cotta, R. M., 2002, "Analytical and Hybrid Solutions of Diffusion Problems Within Arbitrarily Shaped Regions Via Integral Transforms," Comput. Mech., **29**(3), pp. 265–276.
[36] Pinheiro, I. F., Sphaier, L. A., and Knupp, D. C., 2019, "Integral Transform Solution of Eigenvalue Problems Within Irregular Geometries: Comparative Analysis of Different Methodologies," Numer. Heat Transfer, Part B, **76**(6), pp. 329–350.
[37] Pinheiro, I. F., Puccetti, G., Morini, G. L., and Sphaier, L. A., 2021, "Integral Transform Analysis of Microchannel Fluid Flow: Irregular Geometry Estimation Using Velocimetry Data," Appl. Math. Modell., **90**, pp. 943–954.
[38] Serfaty, R., and Cotta, R. M., 1992, "Hybrid Analysis of Transient Nonlinear Convection-Diffusion Problems," Int. J. Numer. Methods Heat Fluid Flow, **2**(1), pp. 55–62.
[39] Cotta, R. M., Knupp, D. C., Naveira-Cotta, C. P., Sphaier, L. A., and Quaresma, J. N. N., 2013, "Unified Integral Transforms Algorithm for Solving Multidimensional Nonlinear Convection-Diffusion Problems," Numer. Heat Transfer, Part A, **63**, pp. 1–27.
[40] Pinheiro, I. F., Sphaier, L. A., and Alves, L. S. B., 2018, "Integral Transform Solution of Integro-Differential Equations in Conduction-Radiation Problems," Numer. Heat Transfer, Part A, **73**(2), pp. 94–114.
[41] Pontes, P. C., Costa Junior, J. M., Naveira-Cotta, C. P., and Tiwari, M. K., 2021, "Approximation Error Model (AEM) Approach With Hybrid Methods in the Forward-Inverse Analysis of the Transesterification Reaction in 3D-Microreactors," Inverse Probl. Sci. Eng., **29**(11), pp. 1586–1612.
[42] Perez-Guerrero, J. S., and Cotta, R. M., 1992, "Integral Transform Solution for the Lid-Driven Cavity Flow Problem in Streamfunction-Only Formulation," Int. J. Numer. Methods Fluids, **15**(4), pp. 399–409.
[43] Lisboa, K. M., and Cotta, R. M., 2018, "Hybrid Integral Transforms for Flow Development in Ducts Partially Filled With Porous Media," Proc. R. Soc. A, **474**, pp. 1–20.
[44] Cruz, C. C. S., Pereira, L. M., Macedo, E. N., Quaresma, J. N. N., and Cotta, R. M., 2021, "Integral Transform Solution of Swirling Laminar Flows in Cylindrical Cavities With Rotating End Walls," J. Braz. Soc. Mech. Sci. Eng., **43**, p. 401.
[45] Cotta, R. M., Lisboa, K. M., Curi, M. F., Balabani, S., Quaresma, J. N. N., Pérez Guerrero, J. S., Macêdo, E. N., and Amorim, N. S., 2019, "A Review of Hybrid Integral Transform Solutions in Fluid Flow Problems With Heat or Mass Transfer and Under Navier–Stokes Equations Formulations," Numer. Heat Transfer, Part B, **76**(2), pp. 60–87.
[46] Alves, L. S. B., and Cotta, R. M., 2000, "Transient Natural Convection Inside Porous Cavities: Hybrid Numerical-Analytical Solution and Mixed Symbolic-Numerical Computation," Numer. Heat Transfer, Part A, **38**(1), pp. 89–110.
[47] Santos, B. M., Sá, L. S. S., and Su, J., 2022, "Natural Convection in a Horizontal Annular Sector Containing Heat-Generating Porous Medium," Int. J. Numer. Methods Heat Fluid Flow, **32**(1), pp. 387–403.
[48] Hirata, S. C., Goyeau, B., Gobin, D., Chandesris, M., and Jamet, D., 2009, "Stability of Natural Convection in Superposed Fluid and Porous Layers: Equivalence of the One- and Two-Domain Approaches," Int. J. Heat Mass Transfer, **52**(1–2), pp. 533–536.
[49] Lisboa, K. M., Zotin, J. L. Z., and Cotta, R. M., 2021, "Hybrid Solutions for Thermally Developing Flows in Channels Partially Filled With Porous Media," Numer. Heat Transfer, Part B, **79**(4), pp. 189–215.
[50] Wolfram, S., 2021, *Wolfram Mathematica 13.0*, Wolfram Research, Champaign, IL.
[51] Alazmi, B., and Vafai, K., 2002, "Constant Wall Heat Flux Boundary Conditions in Porous Media Under Local Thermal Non-Equilibrium Conditions," Int. J. Heat Mass Transfer, **45**(15), pp. 3071–3087.
[52] Almeida, A. R., and Cotta, R. M., 1996, "A Comparison of Convergence Acceleration Schemes for Eigenfunction Expansions of Partial Differential Equations," Int. J. Numer. Methods Heat Fluid Flow, **6**(6), pp. 85–97.
[53] Sphaier, L. A., 2012, "Integral Transform Solution for Heat Transfer in Parallel-Plates Micro-Channels: Combined Electroosmotic and Pressure Driven Flows With Isothermal Walls," Int. Commun. Heat Mass Transfer, **39**(6), pp. 769–775.
[54] Lee, P.-S., Garimella, S. V., and Liu, D., 2005, "Investigation of Heat Transfer in Rectangular Microchannels," Int. J. Heat Mass Transfer, **48**(9), pp. 1688–1704.
[55] Sphaier, L. A., Braga, N. R., and Chalhub, D., 2021, "Analytical Solutions for Extended Graetz Problem in Infinite Domains Via Integral Transforms," Int. J. Therm. Sci., **170**, p. 107093.